Supplementary Material for

Engineering stable construction of $MnCo_2O_4$ yolk-in-double-shell amalgamated with bio-synthesized $ZnMn_2O_4$ nanoparticles for superior artificial CO_2 reduction

Ashkan Bahadoran[a], Jeffrey Roshan De Lile[b], Farzad Hasanvandian[c], Mohammadreza Sharghi[d], Babak Kakavandi[e,f,*], Yogendra Kumar Mishra[g,*], Stefanos Giannakis[h], Seeram Rama Krishna[i,*]

[a] Shenzhen Institutes of Advanced Technology, Chinese Academy of Sciences, Shenzhen 518055, Guangdong, China

[b] Département de physique and Regroupement québécois sur les matériaux de pointe, Université de Montréal, Montréal, Québec H3C3J7, Canada

[c] Department of Chemical and Petroleum Engineering, Sharif University of Technology, Tehran, Iran

[d] Department of Chemistry, Binghamton University, The State University of New York, 4400 Vestal Parkway East, Binghamton, NY, 13902, United States

[e] Research Center for Health, Safety and Environment, Alborz University of Medical Sciences, Karaj, Iran

[f] Department of Environmental Health Engineering, Alborz University of Medical Sciences, Karaj, Iran

[g] SDU NanoSYD, Mads Clausen Institute, University of Southern Denmark, 6400 Sønderborg, Denmark

[h] Universidad Politécnica de Madrid, E.T.S. Ingenieros de Caminos, Canales y Puertos, Departamento de Ingeniería Civil: Hidráulica, Energía y Medio Ambiente, Unidad docente Ingeniería Sanitaria, c/ Profesor Aranguren, s/n, ES-28040 Madrid, Spain

[i] NUS Center for Nanofibers and Nanotechnology, Department of Mechanical Engineering, National University of Singapore, Singapore

1. Experimental

1.1. Materials

All the solvents and reagents, utilized in the current paper, were commercially procured from Merck Company (Darmstadt, Germany) and were used without any additional purification. The ultrapure (>99% purity) form of cobalt nitrate ($Co(NO_3)_2.6H_2O$), manganese nitrite ($Mn(NO_3)_2{\cdot}6H_2O$), and zinc nitrate ($Zn(NO_3)_2{\cdot}6H_2O$) were employed as sources of the Co, Mn, and Zn, respectively. In addition, the

2-propanol (C_3H_8O) and glycerol ($C_3H_8O_3$) as well as Aloe-vera leaves (obtained from local mark) were used as a solvent during photocatalysts fabrication. Other chemicals deployed in the experimental analyses include the triethanolamine (TEOA), acetonitrile (C_2H_3N), sodium sulfate (Na_2SO_4), $[Ru(bpy)_3]Cl_2 \cdot 6H_2O$, and hydrochloric acid (HCl, 37%). The 5 wt.% of D521 Nafion solution was purchased from DuPont company (Delaware, USA). Ultrapure water was utilized during catalyst preparation, CO_2-PR experiments, and all other manipulations.

1.2 Preparation of Aloe-vera gel

The proper numbers of newly picked Aloe-vera leaves were thoroughly washed with ultrapure water for removing all impurities such as dust and related contaminations and then were dried in room temperature. The green rinds of leaves were separated, and inner gels were collected. The obtained gel was blended such that a colloidal solution termed, "AVG" appeared. A proper amount of AVG was mixed with ultrapure water in the three-volume ratio including 40:60 (solution A), 60:40 (solution B), and 80:20 (solution C) and then were stirred at 70 ºC for 30 min. Finally, each solution was separately filtered and kept in the refrigerator at 4 ºC for further usage.

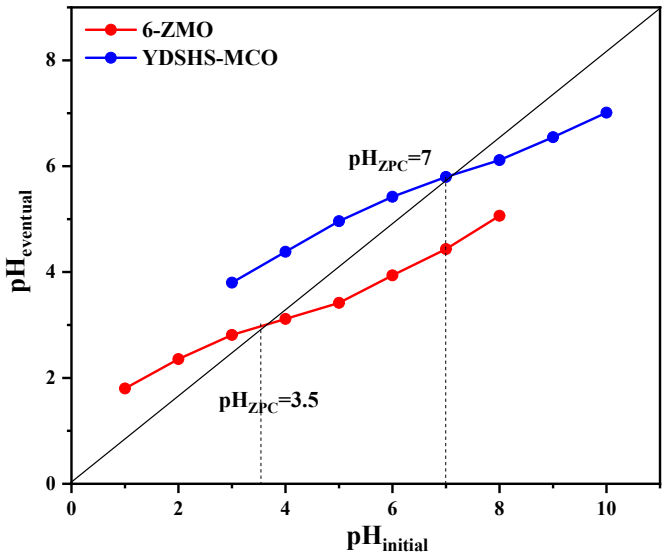

Fig. S1. Variation between beginning pH and ending pH result from drift method for YDSHS-MCO and 6-ZMO samples.

1.3. Photocatalysts characterization techniques

Crystallographic feature attributed to as-constructed nanostructures was specified through Powder X-ray diffraction (XRD) characterization attained from PANalytical XPert Pro MPD, Netherland, which operated under λ = 0.15406 nm, 40 kV, and 30 mA conditions. The valence state and electronic merits of as-fabricated samples were identified via the X-ray photoelectron spectroscopy (XPS) instrument K-alpha XPS spectrometer, Bes Tec, Germany, equipped with 1253.6 eV X-ray power of Mg Kα radiation as an excitation source. The used XPS instrument was calibrated by pure gold (Au $4f_{7/2}$), and separation in calibration energies was adjusted via copper (Cu $2p_{3/2}$ - Cu 3p) based on the International Standards Organization (Document No. ISO 15472:2010: Surface chemical analysis - X-ray photoelectron spectrometers - Calibration of energy scales). In addition, the extent of retardation of carbon adventitious was applied and set at 284.8 eV according to the standard references, as shown in Fig. S2. The morphological elaboration was accomplished using the field emission scanning electron microscopy (FE-SEM) (Mira III, Tescan, Czech Republic) and transmission electron microscope (TEM) images (CM300, PHILIPS, Netherland). The porosity and textural quantification of nanophotocataysts were distinguished through conventional N_2-gas adsorption-desorption under the instrument of BELSORP MINI II, BEL, Japan. The light-harvesting and optical assessments of as-derived samples were conducted with UV-Vis diffuse reflectance spectroscopy (DRS) analysis by Avaspec-2048-TEC spectrophotometer, Avantes, Netherland. The electronic elucidation of charge behavior was described using photoluminescence spectroscopy (PL) characterization under Varian Cary Eclipse, Agilent, USA equipment. In-situ diffuse reflectance infrared Fourier transform spectroscopy (DR-IFTS) was performed by a Bruker INVENIOS FTIR spectrometer.

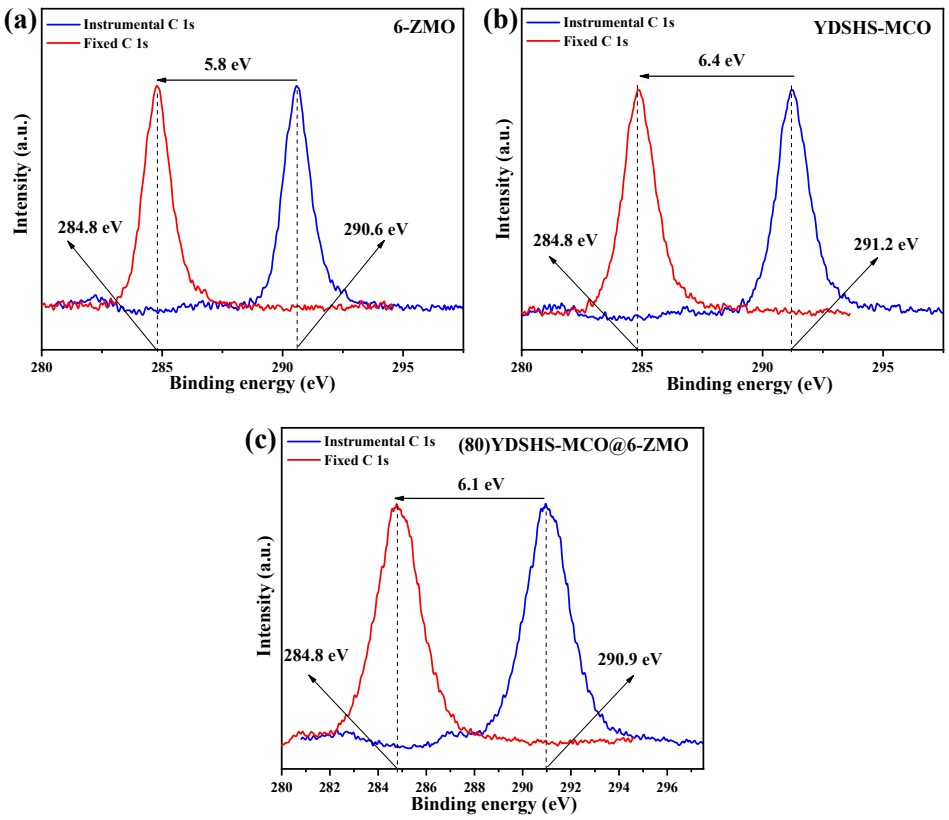

Fig. S2. Arrangement of retardation extent related to carbon adventitious (C 1s) of YDSHS-MCO, 6-ZMO, and (80)YDSHS-MCO@6-ZMO samples.

1.4. Photo/electrochemical measurements

The Compact Electrochemical Interface PalmSens 4 integrated with conventional three-electrode configuration comprising Pt wire (counter electrode), Ag/AgCl (reference electrode) and glassy carbon electrode (working electrode) appraised the intrinsic electrochemical characteristic of as-synthesized nanomaterials. The measurements of electrochemical impedance spectrum (EIS) and Mott-Schottky plots were carried out deploying the mentioned potentiate set-up, while the catalysts-treated glassy carbon electrode (Cat-GCE) was operated as the working electrode with 0.5 M of Na_2SO_4 solution as the electrolyte media. The electrochemical EIS evaluation was recorded in open circuit potential and voltage oscillation of 10 mV within the frequency range of 100 kHz to 0.01 Hz. The Mott–Schottky

curves were acquired under three different frequencies including 0.5, 1, and 1.5 kHz. Besides, in order to effectuate the transient photocurrent (TP), the above-explained procedure was analogous except that the Cat-GCE was substituted with catalyst-modified fluorine doped tin oxide (Cat-FTO) under on/off 300 W of xenon light irradiation. The procedure related to preparation of Cat-GCE and Cat-FTO was thoroughly elaborated was follow:

The even homogenous slurry of catalyst was prepared through mixing 5 mg of certain catalyst, 800 μL of ultrapure water, 170 μL of 2-propanol, and 30 μL of Nafion solution, which was homogenously dispersed under ultrasonic power for 30 min. Subsequently, 1 μL of obtained slurry was casted onto GCE with 2.0 mm diameter so that the catalyst loading reached about 160 mg/mL. Eventually, the catalyst-loaded GCE was left at the ambient condition to uniformly dry and get ready for the subsequent electrochemical analyses. In the case of Cat-FTO, the certain amount of prepared catalyst slurry was evenly dropped onto FTO (1×1 cm^2) and then placed in the ambient condition to remove any solvent and introduce uniform substrate for photoelectrochemical measurements.

1.5. CO_2 photoreduction

1.5.1. Experimental set-up

In order to attain reliable comparison between every single as-fabricated component, the CO_2-PR capability was performed in an acetonitrile-assisted liquid-solid phase reactor under following specific procedure:

The double-shelled cylindrical Pyrex vessel (inside shell dimension: 10 cm in height and 4.6 cm in diameter) was utilized as photoreactor equipped with a quartz window at top of the reactor working as transmit light channel. In addition, inlet and outlet ports was installed on the outside shell so that the water in circulation can keep the temperature of reactor at the specific value. The graphical configuration

of the double liquid-gas phase photoreactor was illustrated in Fig. S3. The reactor content included the 100 mL liquid phase consisting of 4.0 mg of catalysts, 4.0 mL of triethanolamine (TEOA) as sacrificial agent, 10.0 mg of $[Ru(bpy)_3]Cl_2 \cdot 6H_2O$ photosensitizer (abbreviated as Ru-bpy), and 16.0 mL of acetonitrile as well as 50 mL gas phase. A 300 W Xe lamp equipped with cut-off filter was applied as a light source and installed above the quartz window. Prior to starting the irradiation of light source, the ultra-pure CO_2 (99.99 %) was purged and bubbled at liquid phase through the bottom inlet and consequently vented out the reactor through top outlet located at the gas phase. After 1 hour, during which the photoreactor was thoroughly cleaned to remove any other impurities, the reactor ports were sealed, and then the light was turn on. At regular time interval, the specific gaseous content was withdrawn and analyzed utilizing a gas chromatograph (GC). The collected gas samples were identified through a gas chromatograph (GC), Agilent 7890A, which was installed the flame ionization detector (FID), the thermal conductivity detector (TCD), and nickel-packed methanizer in order for conversion CO-to-CH_4. The Ultrapure Helium was chosen as the gas-carrier.

In the interest of appraising the practical usage of CO_2-PR, the CO_2 conversion was accomplished under gas-solid system without applying neither photosensitizer nor sacrificial agents, as described as follow:

The photoreactor configuration was kept the same, whereas catalyst was coated on quartz glass and was placed at the bottom of reactor instead of filling the two-thirds of the reactor with water mixture including catalyst and other agents, as shown in Fig. S5. In detail, 10 mg of catalysis and 1 mL deionized water was uniformly dispersed using ultrasonic energy and then was evenly dropped on the quartz glass (2×2 cm^2). The catalysts-loaded glass was dried in ambient condition, and afterward consequently transferred to the bottom of the reactor, while 1 mL deionized water was added to the reactor. The rest of the procedure was analogous to the earlier described Liquid-solid system.

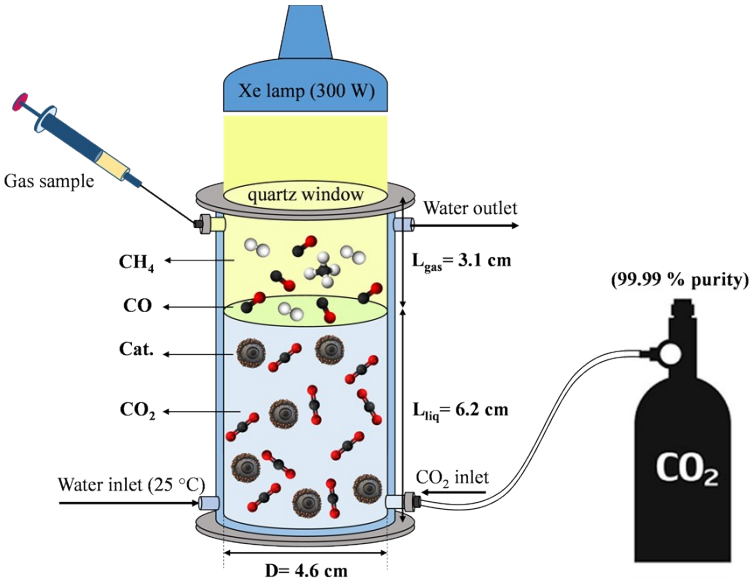

Fig. S3. Schematic presentation of configuration for liquid-solid phase CO_2-PR reactor.

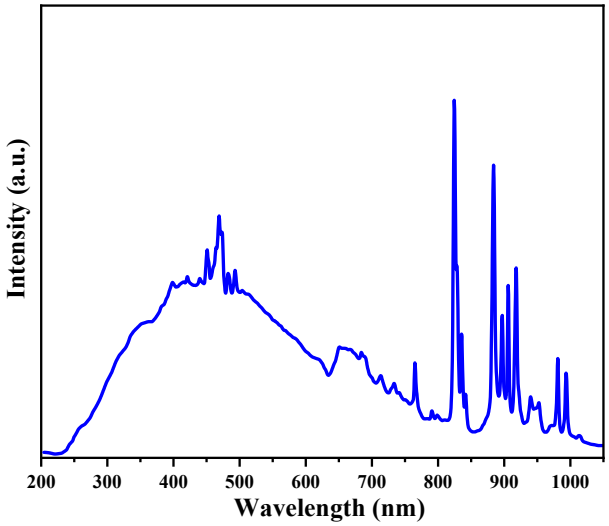

Fig S4. Spectrum of Xe lamp (300 W).

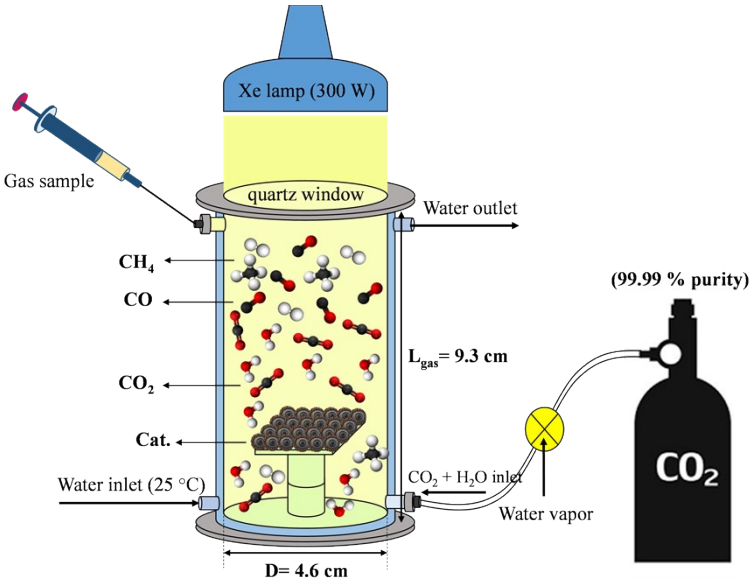

Fig. S5. Schematic presentation of configuration for gas-solid phase CO_2-PR reactor.

1.5.2. Isotopic measurement

Isotopic labelling experiment was accomplished to verify the origination of carbon product which come from CO_2-PR reaction. Therefore, the conventional $^{12}CO_2$ was substituted with $^{13}CO_2$ as the carbon source under analogous process demonstrated in section 1.5.1 in Supplementary Material. However, the produced gaseous products were identified using GC mass spectrometry (GC-MS), Agilent 7890A equipment.

1.5.3. Calculation

1.5.3.1. Scherrer formula

$$D = \frac{K \times \lambda}{\beta \times \cos(\theta)} \quad \text{(S1)}$$

Where, D: crystalline size (nm), K: Shape factor, λ: wavelength of the X-ray, β: width of the diffraction peak, θ: diffraction angle,

1.5.3.2. Bi-exponential function of time-resolved PL

$$I(t) = A_1 \exp(-\frac{t}{\tau_1}) + A_2 \exp(-\frac{t}{\tau_2}) \quad \text{(S2)}$$

$$\tau_{ave.} = \frac{A_1 \tau_1^2 + A_2 \tau_2^2}{A_1 \tau_1 + A_2 \tau_2} \quad \text{(S3)}$$

1.5.3.3. Selectivity

$$\text{Selectivity of CO} = \frac{n_{CO}}{n_{CO} + n_{CH_4} + n_{H_2}} \times 100 \quad \text{(S4)}$$

1.5.3.4. AQE

The apparent quantum efficiency (AQE) of CO production (AQE-CO) related to heterogeneous MCO@6-ZMO was assessed under the as-described conventional reaction system, while the reactor was equipped with a monochromatic irradiation light through which the light irradiation at various specific wavelength (400 ,450, 500, 550, 600, 650, and 700 nm) was provided by band-pass-filtered 300 W Xe lamp.

$$\text{AQE (\%)} = \frac{\text{Number of effective photons}}{\text{Number of total photons}} \times 100 \quad \text{(S5)}$$

$$\text{AQE(\%)} = \frac{\text{Number of CO/H}_2\text{ molecules} \times 2}{\text{Number of total photon}} \times 100 \quad \text{(S6)}$$

$$\text{AQE(\%)} = \frac{(Y_{CO} + Y_{H_2}) \times N_A \times 2}{P \times S \times t \times \frac{\lambda}{hc}} \times 100 \quad \text{(S7)}$$

Where Y_{CO}: production yield of CO (μmol), Y_{H2}: production yield of H_2 (μmol), N_A: Avogadro constant (6.02×10^{23} 1/mol), S: irradiated area (16.5 cm^2), λ: the monochromatic wavelength of irradiated light (400, 450, 500, 550, 600, 650, and 700 nm), h: Planck constant (6.626×10^{-34} J.s), and c: the speed of

light (3×10^8 m/s). In addition, the average light intensity (P) was assessed through optical power meter (Beijing Perfectlight).

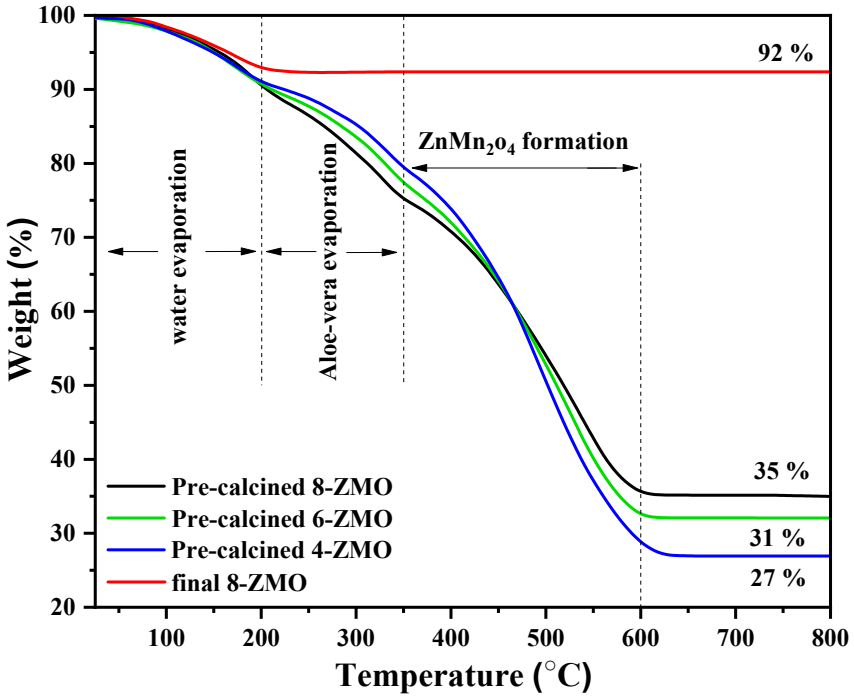

Fig. S6. TGA profiles of pre-calcined 4-ZMO, 6-ZMO, 8-ZMO, and final 6-ZMO samples.

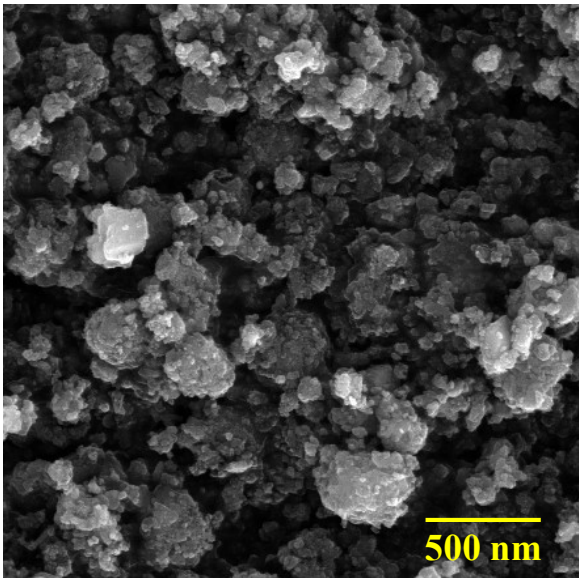

Fig. S7. The FE-SEM photograph of C-ZMO nanoparticles.

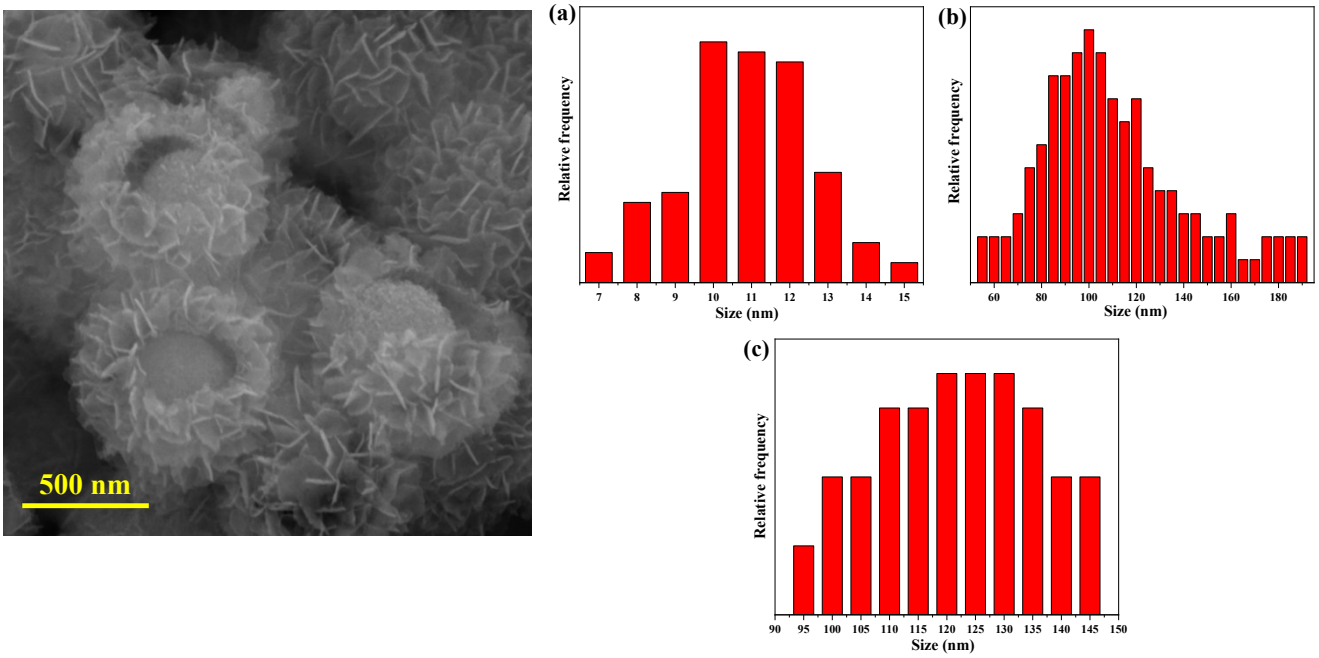

Fig. S8. The size distribution of thickness (a), length (b), and depth (c) of the nanosheet-assembled exterior shell of YDSHS-MCO structure.

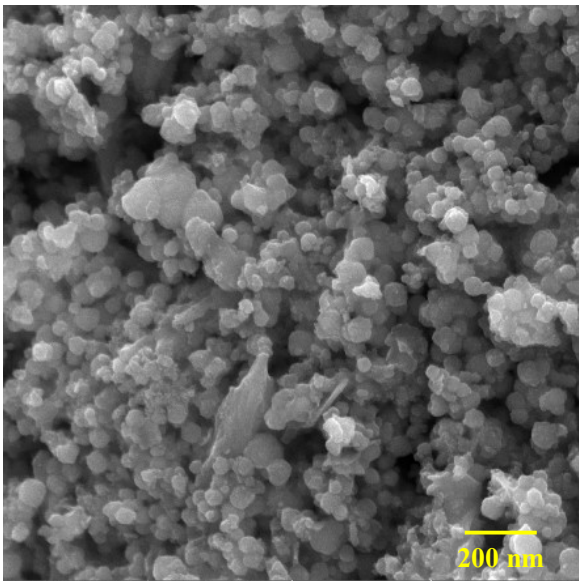

Fig. S9. The FE-SEM image of NP-MCO nanoparticles.

Fig. S10. The size distribution curve for 4-ZMO, 6-ZMO, and 8-ZMO samples.

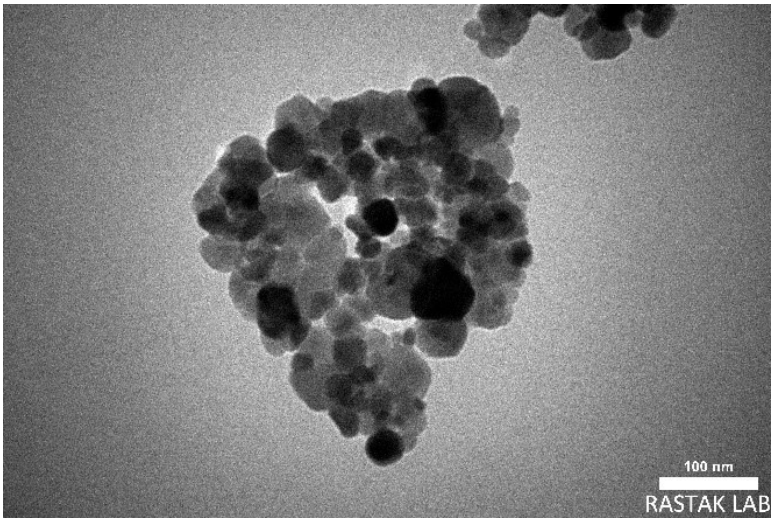

Fig. S11. The TEM image for C-ZMO nanoparticles.

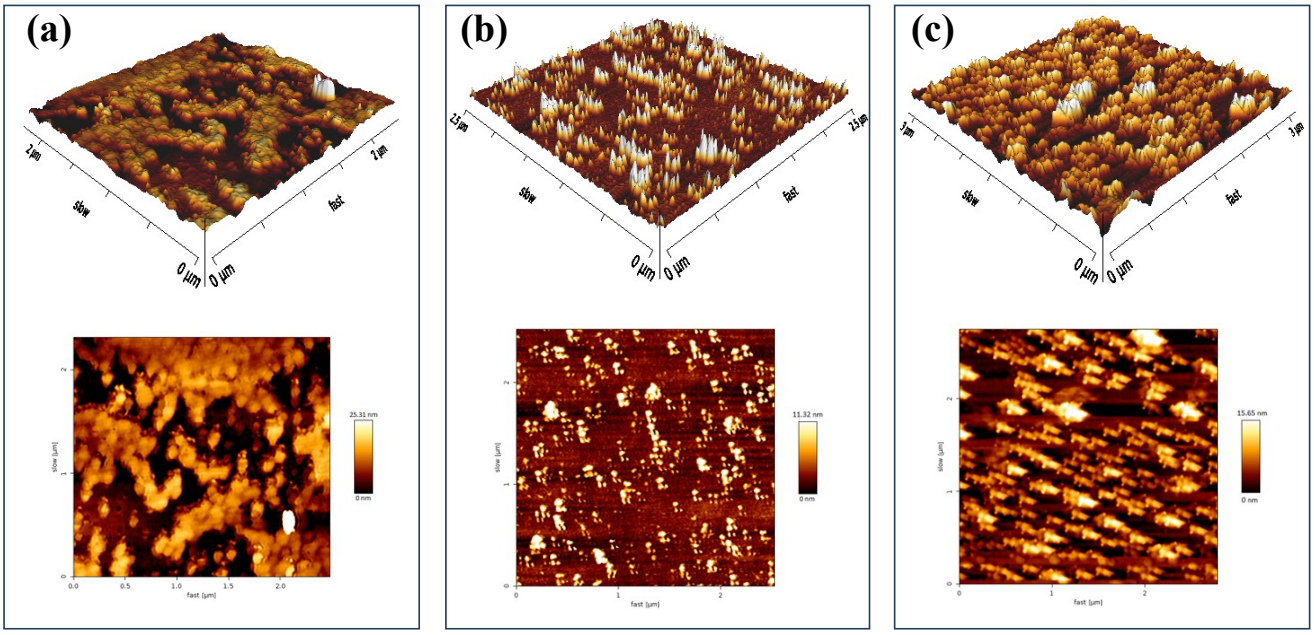

Fig. S12. The AFM analysis related to (a) 4-ZMO, (b) 6-ZMO, and (c) 8-ZMO samples.

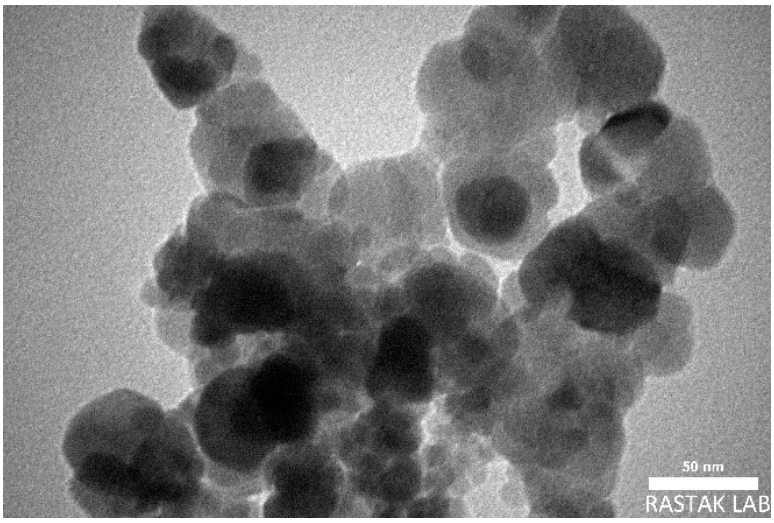

Fig. S13. The TEM photograph for NP-MCO nanoparticles.

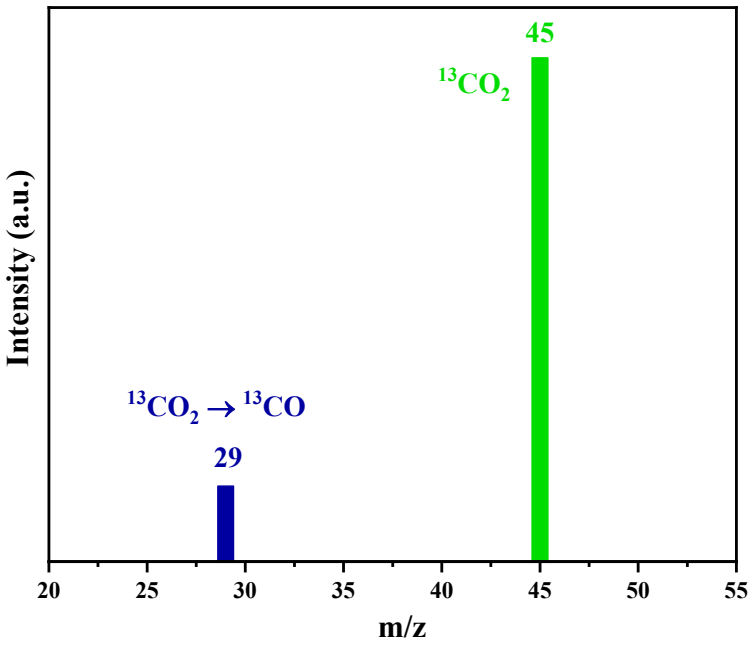

Fig. S14. Mass spectra of generated ^{13}CO under atmosphere of $^{13}CO_2$ as the carbon source of CO-PR reaction.

Fig. S15. (a) The transformation yields of CO_2-to-CH_4 and (b) time evolution curves of CH_4 production attributed to various samples under liquid-solid phase reaction.

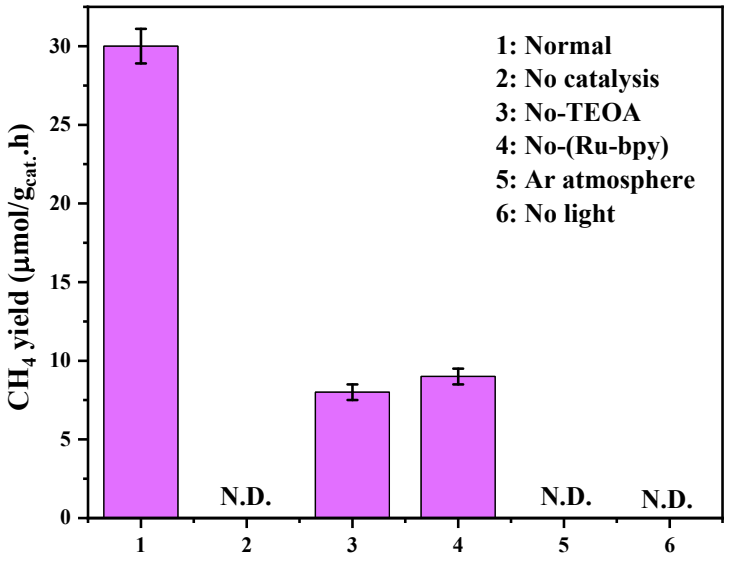

Fig. S16. The results of control experiment for CH_4 production related to the (80)YDSHS-MCO@6-ZMO sample.

Fig. S17. The time course of CO (a), H_2 (b), and O_2 (c) production related to various catalysts under gas-solid phase CO_2-PR reaction.

Fig. S18. (a) The conversion yields of CO_2-to-CH_4 and (b) its corresponding time evolution curves attributed to diverse catalysts under gas-solid phase condition.

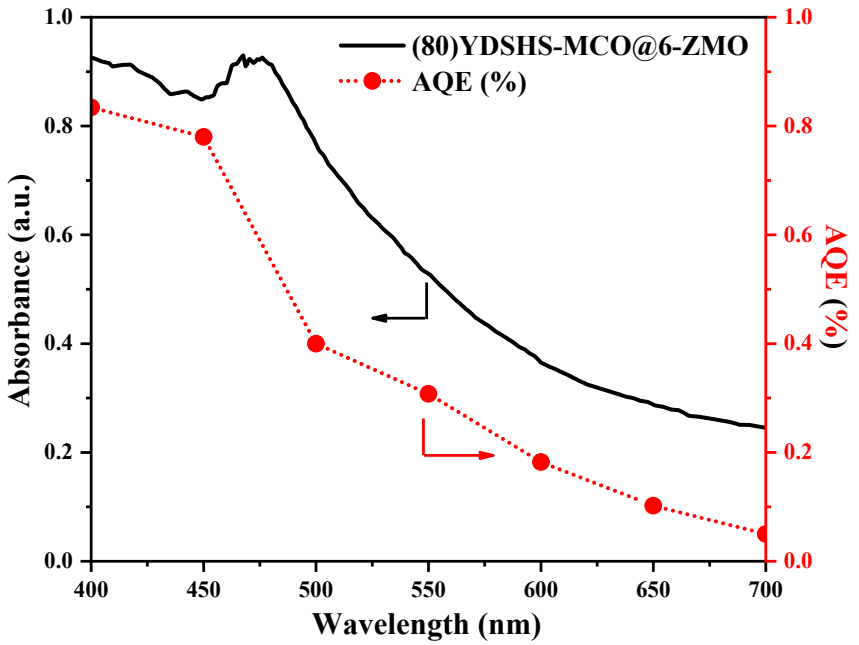

Fig. S19. Wavelength-dependency of AQE to the light absorption capability of YDSHS-MCO@6-ZMO in gas-solid reaction.

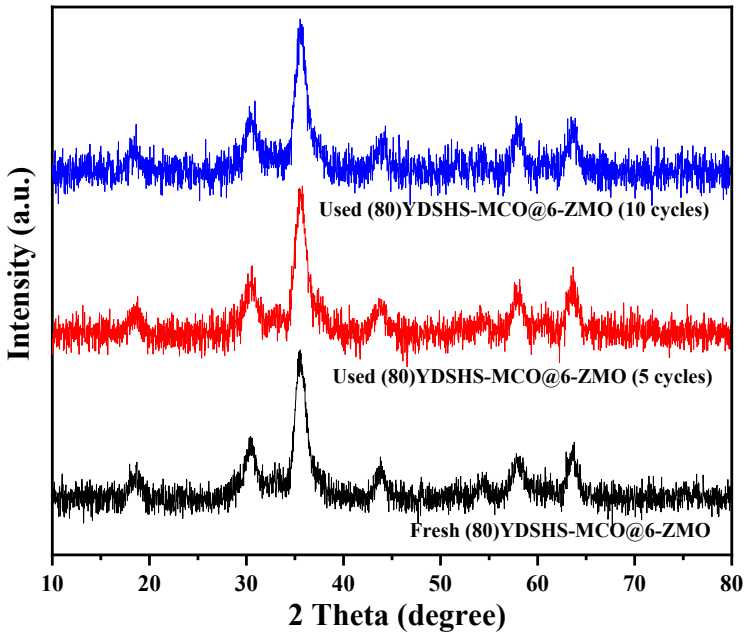

Fig. S20. The XRD spectrum of pre- and post- long-term liquid-solid phase reaction attributed to (80)YDSHS-MCO@6-ZMO nanocomposite.

Fig. S21. Post XPS spectra of (80)YDSHS-MCO@6-ZMO after long-term liquid-solid phase reaction.

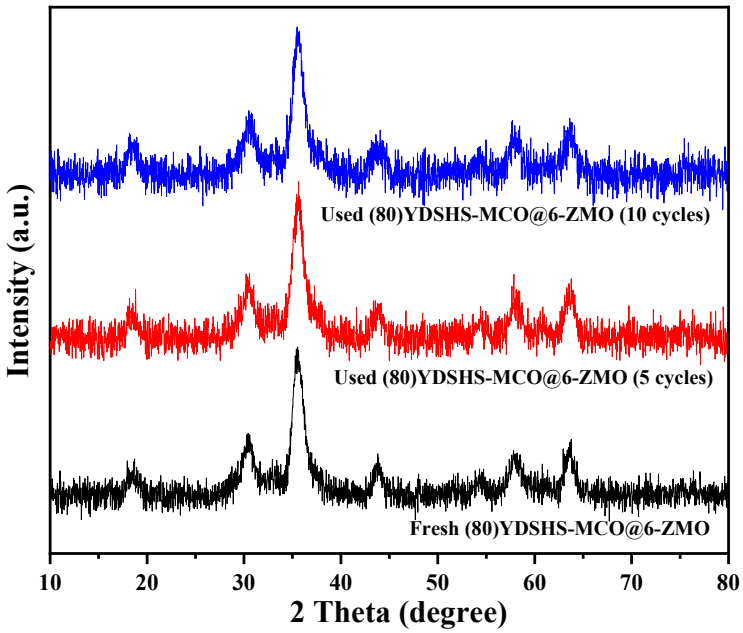

Fig. S22. The XRD spectrum of pre- and post- long-term gas-solid phase reaction attributed to (80)YDSHS-MCO@6-ZMO nanocomposite.

Fig. S23. Post XPS spectra of (80)YDSHS-MCO@6-ZMO after long-term gas-solid phase reaction.

Table S1. Comparison of the reported specific surface area attributed to $ZnMn_2O_4$ nanoparticles with the as-synthesized 6-ZMO in present research.

Sample	**$S_{(BET)}$ (m^2/g)**	**V_p (cm^3/g)**	**Ref.**
$ZnMn_2O_4$ nanoparticles	19.1	-	Frontiers of Chemical Science and Engineering volume (2020) [13]
$ZnMn_2O_4$ nanoparticles	23.9	0.10	Journal of Alloys and Compounds (2021)

			[14]
$ZnMn_2O_4$ nanoparticles	45.1	-	Journal of Alloys and Compounds (2021) [15]
$ZnMn_2O_4$ nanoparticles	45.9	-	Journal of Alloys and Compounds (2016) [16]
$ZnMn_2O_4$ nanoparticles	67.0	0.13	Materials Science & Engineering B (2020) [17]
MOF-driven $ZnMn_2O_4$ nanoparticles	109.1	0.31	Applied Surface Science (2019) [18]
6-ZMO	**128**	**0.91**	**This study**

Table S2. Comparison of the reported specific surface area attributed to multi-shelled materials with the as-synthesized YDSHS-MCO in present research.

Sample	**$S_{(BET)}$ (m^2/g)**	**V_p (cm^3/g)**	**Ref.**
$NiCo_2S_4$ ball-in-ball hollow spheres	53.9	0.18	Nature Communications (2015) [1]
hierarchical flower-like $MnCo_2O_4$	134	0.18	Applied Surface Science (2021) [2]
hierarchical $MnCo_2O_4$ yolk-shell spheres.	129	0.37	Chemical Engineering Journal (2021) [3]
Multilayer Hollow $MnCo_2O_4$ Microsphere	17.3	-	Chemical Engineering Journal (2021) [4]
Mg-doped $CaCO_3$ triple-shelled hollow microspheres	25	0.14	Chemical Engineering Journal (2017) [5]
Hierarchical Triple-Shelled $MnCo_2O_4$ Hollow Microspheres	31.1	0.13	Small (2021) [6]
$CoMn_2O_4$ hollow spheres	82.6	0.16	Catalysis Today (2020) [7]
Co-Mn mixed oxide double shelled hollow spheres	49.5	0.39	Journal of Materials Chemistry A (2019) [8]

Triple-shelled V_2O_5 hollow spheres	28.3	48	Nature Energy (2017) [9]
$MnCo_2O_4$ yolk-in-double shell structures	36.40	-	Applied materials and interfaces (2014) [10]
Co-Mn Prussian Blue Analog Hollow Spheres	89.8	0.29	Angewandte Chemie International Edition (2021) [11]
multi-shelled $MnCo_2O_4$ hollow sphere	203	0.29	iScience (2019) [12]
YDSHS-MCO	**327**	**0.91**	**This study**

Table S3. The extracted parameters of time-resolved PL related to various samples resulting from fitting with bi-exponential function.

sample	**T_1**	**A_1**	**T_2**	**A_2**	**$T_{ave.}$**
YDSHS-MCO	1.5	10	4.1	25	3.77
NP-MCO	0.6	6	2.3	17	2.15
C-ZMO	0.4	6	2.1	17	2.0
4-ZMO	0.9	6	2.5	18	2.32
6-ZMO	1.3	9	3.4	23	3.12
8-ZMO	1.1	7	2.8	21	2.59
(80)YDSHS-MCO@6-ZMO	3.4	10	10.7	26	9.90

Table S4. Details of fitting EIS data related to the equivalent circuit model as illustrated in the insert of Fig. 6(f).

sample	R_s	C_{dl}	R_{ct}
C-ZMO	40	0.056	1396
4-AMO	44	0.059	1274
6-ZMO	44	0.055	992

8-ZMO	44	0.058	1052
NP-MCO	44	0.055	1346
YDSHS-MCO	41	0.052	900
(80)YDSHS-MCO@6-ZMO	40	0.044	326

Table S5. Comparison study between the present research and recently reported state-of-the-art catalysts.

catalyst	**Light source**	**Reaction phase**	**Reaction conditions**	**AQE (%)**	**Yields rate of products (μmol/g.h)**	**Ref.**
MOF-Derived $Ni_{0.2}Co_{0.8}O$ microrod	300 W Xe ($\lambda > 400$ nm)	Liquid-solid	$[Ru(bpy)_3]Cl_2 \cdot 6H_2O$ TEOA DMF	2.39 (480 nm)	CO: 277 H_2: 48	Small 2022 [19]
$NiCo_2O_4$ hollow nanocages	5W LED light (400–800 nm)	Liquid-solid	$[Ru(bpy)_3]Cl_2 \cdot 6H_2O$ TEOA acetonitrile	1.86 (420 nm)	CO: 1400 H_2: 92	Applied Catalysis B: Environmental 2020 [20]
Defective g-C_3N_4/COF	300 W Xe ($\lambda > 400$ nm)	Liquid-solid	$[Ru(bpy)_3]Cl_2 \cdot 6H_2O$ TEOA acetonitrile	-	CO: 562 H2: 56	Applied Catalysis B: Environmental 2022 [21]
$ZnIn_2S_4$/g-C_3N_4	300 W Xe	Liquid-solid	$[Ru(bpy)_3]Cl_2 \cdot 6H_2O$ TEOA acetonitrile	-	CO: 883 H_2: 71	Chemical Engineering Journal 2022 [22]
Cu_2S@ROH-$NiCo_2O_3$	300 W Xe ($\lambda > 400$ nm)	Liquid-solid	$[Ru(bpy)_3]Cl_2 \cdot 6H_2O$ TEOA acetonitrile	-		Angewandte Chemie 2022 [23]

Hollow Multi-Shelled Co_3O_4 Dodecahedron	200 W Xe lamp	Gas-solid	-	0.017 (350 nm)	CO: 46.3 O_2: 25	JACS 2019 [24]
CoPc/BiOBr-NSs	UV–vis light (200 mW/cm^2)	Gas-solid	-	-	CO: 59.43 CH_4: 6.33	Chemical Engineering Journal 2023 [25]
TiO_2/$CsPbBr_3$	300 W Xe	Gas-solid	-	-	CO: 13.49 H_2: 0.43	Nature Communications 2020
		Liquid-solid		-	CO: 2065 H_2: 70	
Hollow quadruple-shelled CeO_2/ amorphous TiO_2	300 W Xe	Gas-solid	-	-	CO: 43	Angewandte Chemie 2022 [26]
layer-structured $Bi_2O_2(OH)(NO_3)$-Br	300 W Xe	Gas-solid	-	-	CO: 8.12	Adv. Mater. 2019 [27]
(80)YDSHS-MCO@6-ZMO	**300 W Xe (λ > 400 nm)**	**Liquid-solid**	**[Ru(bpy)$_3$] Cl_2·6H_2O TEOA acetonitrile**	**2.1 (450 nm)**	**CO:1253 H_2:158**	**This study**
		Gas-solid	**-**	**0.84 (400 nm)**	**CO: 72** (Or 1800 μmol/cm^2.h) **H_2: 13** (Or 325 μmol/cm^2.h)	

References

[1] L. Shen, L. Yu, H. Bin Wu, X.-Y. Yu, X. Zhang, X.W.D. Lou, Formation of nickel cobalt sulfide ball-in-ball hollow

spheres with enhanced electrochemical pseudocapacitive properties, Nat. Commun. 6 (2015) 1–8.

[2] Y. Zhu, X. Xiao, J. Wang, C. Ma, X. Jia, W. Qiao, L. Ling, Enhanced activity and water resistance of hierarchical flower-like Mn-Co binary oxides for ammonia-SCR reaction at low temperature, Appl. Surf. Sci. 569 (2021) 150989.

[3] Y.V. Kaneti, Y. Guo, N.L.W. Septiani, M. Iqbal, X. Jiang, T. Takei, B. Yuliarto, Z.A. Alothman, D. Golberg, Y. Yamauchi, Self-templated fabrication of hierarchical hollow manganese-cobalt phosphide yolk-shell spheres for enhanced oxygen evolution reaction, Chem. Eng. J. 405 (2021) 126580.

[4] K. Zeng, W. Li, Y. Zhou, Z. Sun, C. Lu, J. Yan, J.-H. Choi, R. Yang, Multilayer hollow MnCo2O4 microsphere with oxygen vacancies as efficient electrocatalyst for oxygen evolution reaction, Chem. Eng. J. 421 (2021) 127831.

[5] J. Feng, H. Guo, S. Wang, Y. Zhao, X. Ma, Fabrication of multi-shelled hollow Mg-modified CaCO3 microspheres and their improved CO2 adsorption performance, Chem. Eng. J. 321 (2017) 401–411.

[6] R. Huang, J. Lin, J. Zhou, E. Fan, X. Zhang, R. Chen, F. Wu, L. Li, Hierarchical Triple-Shelled MnCo2O4 Hollow Microspheres as High-Performance Anode Materials for Potassium-Ion Batteries, Small. 17 (2021) 2007597.

[7] L. Ding, W. Yang, L. Chen, H. Cheng, Z. Qi, Fabrication of spinel CoMn2O4 hollow spheres for highly selective aerobic oxidation of 5-hydroxymethylfurfural to 2, 5-diformylfuran, Catal. Today. 347 (2020) 39–47.

[8] Y. Guo, C. Wu, N.-W. Li, S. Yuan, L. Yu, Formation of Co–Mn mixed oxide double-shelled hollow spheres as advanced electrodes for hybrid supercapacitors, J. Mater. Chem. A. 7 (2019) 25247–25253.

[9] J. Wang, H. Tang, L. Zhang, H. Ren, R. Yu, Q. Jin, J. Qi, D. Mao, M. Yang, Y. Wang, Multi-shelled metal oxides prepared via an anion-adsorption mechanism for lithium-ion batteries, Nat. Energy. 1 (2016) 1–9.

[10] J. Li, J. Wang, X. Liang, Z. Zhang, H. Liu, Y. Qian, S. Xiong, Hollow MnCo2O4 submicrospheres with multilevel interiors: from mesoporous spheres to yolk-in-double-shell structures, ACS Appl. Mater. Interfaces. 6 (2014) 24–30.

[11] Y. Zeng, X.F. Lu, S.L. Zhang, D. Luan, S. Li, X.W. Lou, Construction of Co–Mn Prussian Blue Analog Hollow Spheres for Efficient Aqueous Zn-ion Batteries, Angew. Chemie Int. Ed. 60 (2021) 22189–22194.

[12] Z. Xu, Y. Zhang, X. Li, L. Qin, Q. Meng, G. Zhang, Z. Fan, Z. Xue, X. Guo, Q. Liu, Template-free synthesis of stable cobalt manganese spinel hollow nanostructured catalysts for highly water-resistant CO oxidation, Iscience. 21 (2019) 19–30.

[13] Q. Ni, H. Cheng, J. Ma, Y. Kong, S. Komarneni, Efficient degradation of orange II by ZnMn 2 O 4 in a novel photo-chemical catalysis system, Front. Chem. Sci. Eng. 14 (2020) 956–966.

[14] C. Chen, Y. Huang, Q. Fang, S. Wang, Preparation of C, Sn modified ZnMn2O4 porous microsphere and its electrochemical performance, J. Alloys Compd. 889 (2021) 161654.

[15] R. Gherbi, M. Benamira, Y. Bessekhouad, Enhanced photoelectrochemical and photocatalytic properties of Mg-doped ZnMn2O4, J. Alloys Compd. 851 (2021) 156797.

[16] R. Gherbi, Y. Bessekhouad, M. Trari, Structure, optical and transport properties of Mg-doped ZnMn2O4, J. Alloys Compd. 655 (2016) 188–197.

[17] K. Aruchamy, R. Nagaraj, H.M. Manohara, M.R. Nidhi, D. Mondal, D. Ghosh, S.K. Nataraj, One-step green route synthesis of spinel ZnMn2O4 nanoparticles decorated on MWCNTs as a novel electrode material for supercapacitor, Mater. Sci. Eng. B. 252 (2020) 114481.

[18] S. Yan, Y. Yu, Y. Cao, Synthesis of porous ZnMn2O4 flower-like microspheres by using MOF as precursors and its application on photoreduction of CO2 into CO, Appl. Surf. Sci. 465 (2019) 383–388.

[19] H. Yang, D. Zhang, Y. Luo, W. Yang, X. Zhan, W. Yang, H. Hou, Highly Efficient and Selective Visible-Light Driven Photoreduction of CO2 to CO by Metal–Organic Frameworks-Derived Ni□ Co□ O Porous Microrods, Small. 18 (2022) 2202939.

[20] B. Han, J. Song, S. Liang, W. Chen, H. Deng, X. Ou, Y.-J. Xu, Z. Lin, Hierarchical NiCo2O4 hollow nanocages for photoreduction of diluted CO2: Adsorption and active sites engineering, Appl. Catal. B Environ. 260 (2020) 118208.

[21] J. Wang, Y. Yu, J. Cui, X. Li, Y. Zhang, C. Wang, X. Yu, J. Ye, Defective g-C3N4/covalent organic framework van der Waals heterojunction toward highly efficient S-scheme CO2 photoreduction, Appl. Catal. B Environ. 301 (2022) 120814.

[22] L. Li, D. Ma, Q. Xu, S. Huang, Constructing hierarchical ZnIn2S4/g-C3N4 S-scheme heterojunction for boosted CO2 photoreduction performance, Chem. Eng. J. 437 (2022) 135153.

[23] L. Li, X. Dai, D. Chen, Y. Zeng, Y. Hu, X.W. Lou, Steering Catalytic Activity and Selectivity of CO2 Photoreduction to Syngas with Hydroxy-Rich Cu2S@ ROH-NiCo2O3 Double-Shelled Nanoboxes, Angew. Chemie Int. Ed. 61 (2022) e202205839.

[24] L. Wang, J. Wan, Y. Zhao, N. Yang, D. Wang, Hollow multi-shelled structures of Co3O4 dodecahedron with unique crystal orientation for enhanced photocatalytic CO2 reduction, J. Am. Chem. Soc. 141 (2019) 2238–2241.

[25] W. Li, X. Li, X. Fu, Z. Lou, Y. Zhu, Y. Zhang, Photo-induced conversion of type-II CoPc/BiOBr-NSs to S-scheme heterostructure for boosting CO2 photoreduction, Chem. Eng. J. 451 (2023) 138932.

[26] Y. Wei, F. You, D. Zhao, J. Wan, L. Gu, D. Wang, Heterogeneous Hollow Multi-Shelled Structures with Amorphous-Crystalline Outer-Shells for Sequential Photoreduction of CO2, Angew. Chemie Int. Ed. 61 (2022) e202212049.

[27] L. Hao, L. Kang, H. Huang, L. Ye, K. Han, S. Yang, H. Yu, M. Batmunkh, Y. Zhang, T. Ma, Surface-halogenation-induced atomic-site activation and local charge separation for superb CO2 photoreduction, Adv. Mater. 31 (2019) 1900546.